Nomura et al. Progress in Earth and Planetary Science (2017) 4:34
DOI 10.1186/s40645-017-0149-2

Progress in Earth and Planetary Science

RESEARCH ARTICLE Open Access

Melting phase relations in the $MgSiO_3$–$CaSiO_3$ system at 24 GPa

Ryuichi Nomura[1*], Youmo Zhou[1*] and Tetsuo Irifune[1,2]

Abstract

The Earth's lower mantle is composed of bridgmanite, ferropericlase, and $CaSiO_3$-rich perovskite. The melting phase relations between each component are key to understanding the melting of the Earth's lower mantle and the crystallization of the deep magma ocean. In this study, melting phase relations in the $MgSiO_3$–$CaSiO_3$ system were investigated at 24 GPa using a multi-anvil apparatus. The eutectic composition is (Mg,Ca)SiO_3 with 81–86 mol% $MgSiO_3$. The solidus temperature is 2600–2620 K. The solubility of $CaSiO_3$ component into bridgmanite increases with temperature, reaching a maximum of 3–6 mol% at the solidus, and then decreases with temperature. The same trend was observed for the solubility of $MgSiO_3$ component into $CaSiO_3$-rich perovskite, with a maximum of 14–16 mol% at the solidus. The asymmetric regular solutions between bridgmanite and $CaSiO_3$-rich perovskite and between $MgSiO_3$ and $CaSiO_3$ liquid components well reproduce the melting phase relations constrained experimentally.

Keywords: Bridgmanite, $CaSiO_3$-rich perovskite, Melting phase relations, Multi-anvil experiments, High pressure and high temperature, Thermodynamics

Introduction

Determining melting phase relations in natural rock-forming, multi-component systems at high pressures is essential to understand the origin and consequences of the deep mantle melting (e.g., Williams and Garnero 1996) and the crystallization of the deep magma ocean of the early Earth (e.g., Ito et al. 2004). Although numerous melting experiments have been performed for these purposes, the range of parameter space (pressure (P), temperature (T), and compositions (X)) studied is limited for tracing the crystallization of the magma ocean and for a comprehensive investigation into the origin of the deep mantle melting. Indeed, it is not practical to cover the vast P–T–X space relevant to deep Earth events based on experiments alone. In contrast, experiments in simpler systems combined with thermodynamic models provide a powerful tool to understand the melting chemistry in the multi-component system. Such comprehensive datasets and thermodynamic models have been constructed for pressures up to those of the mantle transition zone (Gasparik 2003).

In addition, the occurrence of a certain degree of temperature gradient is inevitable in melting experiments using laser-heated diamond anvil cells or multi-anvil apparatuses, especially under the high pressures of the lower mantle. The temperature gradient obscures the melting chemistry in multi-component systems because phase segregation changes the bulk compositions of interest. In these cases, only limited information, such as phase equilibria and element partitioning between the phases in contact, can be extracted by assuming local chemical equilibrium. This problem could be overcome by experiments in simple binary systems.

The lower mantle is composed of bridgmanite, ferropericlase, and $CaSiO_3$-rich perovskite (Irifune 1994). Normal mid-ocean ridge basalt has a mineral assemblage of bridgmanite, $CaSiO_3$-rich perovskite, a SiO_2 phase, and an aluminous phase in the lower mantle (Hirose et al. 1999). Therefore, the binary melting phase relations between each mineral-constituting component are important in understanding the melting behaviors of the lower mantle. Previously, the MgO–$MgSiO_3$ system was investigated at the lower-mantle pressures using a multi-anvil press (Liebske and Frost 2012), but little is known about the other systems.

* Correspondence: nomura@sci.ehime-u.ac.jp; youmo@sci.ehime-u.ac.jp
[1]Geodynamics Research Center, Ehime University, 2-5 Bunkyo, Matsuyama, Ehime 790-8577, Japan
Full list of author information is available at the end of the article

This paper is aimed at establishing the melting phase relations in the $MgSiO_3$–$CaSiO_3$ system at 24 GPa, avoiding ambiguous implications for Earth science that require other melting phase relations such as MgO–$CaSiO_3$. The eutectic composition, solidus temperature, and solubility between the two endmembers were investigated experimentally at 24 GPa. Although Gasparik (1996) has performed a melting experiment on the same system at 22.4 GPa, it is difficult to confirm melting from the backscattered electron image presented in his paper. In the present work, we re-investigate the system to find the interaction parameters between the $MgSiO_3$ and $CaSiO_3$ components by thermodynamic analysis in the framework for the endmembers (de Koker and Stixrude 2009; Stixrude and Lithgow-Bertelloni 2011; Bajgain et al. 2015) consistent with a previous work in the MgO-$MgSiO_3$ system (Liebske and Frost 2012).

Methods/experimental

Starting materials

We used three starting compositions, i.e., $Mg_{0.90}Ca_{0.10}SiO_3$ (Mg90), $Mg_{0.75}Ca_{0.25}SiO_3$ (Mg75), and $Mg_{0.50}Ca_{0.50}SiO_3$ (Mg50). Bubble-free, chemically homogenous glasses were synthesized for $Mg_{0.75}Ca_{0.25}SiO_3$ and $Mg_{0.50}Ca_{0.50}SiO_3$ in Pt crucibles at 2023 K using chemical mixtures of SiO_2 (99.9%, Kojundo Chemical Laboratory Co., Ltd.), MgO (> 99.99%, Kojundo Chemical Laboratory Co., Ltd.), and $CaCO_3$ (> 98.0%, Kanto Chemical Co., Inc.), after decarbonation at 1273 K for 16 h. The starting material with a bulk composition of $Mg_{0.90}Ca_{0.10}SiO_3$ was not vitrified completely, which is likely because of its high Mg content. We crushed and ground it to fine particles. The bulk composition of the latter starting material was confirmed via electron microprobe analysis after a subsolidus high-pressure and high-temperature experiment. Table 1 lists the bulk compositions of the starting materials. The starting materials were stored in a furnace at 383 K before use.

High-pressure melting experiments

High-pressure and high-temperature experiments were performed at 24 GPa and 2600–3000 K in a Kawai-type multi-anvil apparatus (Orange 2000, Geodynamics Research Center, Ehime University). A 10/4 (octahedron edge length/truncation edge length) cell assembly was chosen for pressure generation. The pressure of 24 GPa was calibrated based on the coexistence and dissociation of wadsleyite into bridgmanite and periclase at 2273 K in the Mg_2SiO_4 system (Fei et al. 2004), in addition to other phase transitions at room temperature, 1873 and 2273 K, as described in Zhou et al. (2017). The pressure calibration (Additional file 1: Figure S1) suggests that pressure does not vary with temperature above 1873 K. This is also evidenced by the recovery of bridgmanite from 2620 K (OS3099) since the pressure drop of less than 2 GPa is needed to be within the stability field of bridgmanite at that temperature (Gasparik 1996; Fei et al. 2004). A $LaCrO_3$ heater was chosen for temperature generation. The temperature was monitored with a $W_{97}Re_3$-$W_{75}Re_{25}$ thermocouple. No correction was applied for the pressure effect on the electromotive force of the thermocouple. The junction of the thermocouple was positioned at the center of the heater and between two Re capsules. The cell assembly used in this study is identical to that of Zhang et al. (1993) with respect to the octahedron dimension (edge length, 10 mm), the heater material ($LaCrO_3$), and the capsule material (Re). However, we used capsules with much smaller dimensions in both length and diameter and adopted a longer sleeve heater with a much smaller diameter to reduce the thermal gradient. Zhang et al. (1993) reported a temperature drop of ~ 50 K at a distance of ~ 0.5 mm from the hot spot axially. In this study, the center of the sample (~ 0.2 mm thick) is ~ 0.5 mm away axially from the thermocouple junction. Therefore, the uncertainty of the sample temperature caused by the temperature gradient is much less than 50 K. Indeed, we confirmed drastic changes of the melting phase relations within 100 K in a series of experiments. In addition, the obtained electron microprobe images of the recovered samples suggest that the thermal gradient in the axial direction was negligible and it was not the dominant factor of temperature uncertainty (i.e., no systematic error). Therefore, small, non-systematic changes in the geometry and temperature profile caused by the differences in the geometry of components (heater shape and size, the degree of cell deformation during heating, and so on) in each run lead to uncertainties in temperature. We adopted the variations in the heating power-temperature relationships (Additional file 1: Figure S2) as temperature uncertainties, although they represent the variations not only in the thermocouple-sample geometry and temperature profile but also in other factors not related to the temperature uncertainty but to the heating efficiency. Therefore, uncertainties would be overestimated. However, this is the best way to express the uncertainties in experimental temperatures (Table 2). The high-pressure samples were quenched by cutting off the power supply at the target temperatures after heating for 5–20 min. The experimental conditions and results are summarized in Table 2.

Phase identification and chemical analysis

The recovered samples were embedded in epoxy resin and finely polished for subsequent analyses. Phase identification was conducted with a microfocus X-ray diffraction (XRD) apparatus (Rigaku MicroMax-007HF) using Cu Kα radiation. The sample surface was coated with carbon and analyzed using a field emission-type scanning electron microscope (FE-SEM; JEOL JSM7000F).

Table 1 Chemical compositions of starting materials

Name	Phase[a]	MgO	CaO	SiO_2	Total (wt.%)	Mg	Ca	Si	∑Cation[b]	Mg/(Mg + Ca)
Mg90	Mixture	35.63(22)	5.30(45)	58.87(54)	99.79(33)	0.903(1)	0.097(9)	1.001(4)	2.000(4)	0.904(8)
Mg75	Glass (29)	28.99(22)	13.67(10)	57.12(42)	99.78(50)	0.753(5)	0.255(2)	1.004(2)	2.004(3)	0.747(2)
Mg50	Glass (26)	18.53(16)	25.65(15)	54.89(36)	99.07(59)	0.503(3)	0.500(2)	0.999(2)	2.001(2)	0.501(2)

[a]Number of electron microprobe analyses is shown in parentheses. Mg90 is a mixture of glass and oxides; see the main text for details
[b]Number of oxygen is 3

Chemical compositions were measured using an energy-dispersive X-ray spectrometer with a silicon-drift detector (EDS; Oxford Instruments X-Max^N) attached to the FE-SEM at 15 kV and 1 nA with collection times of ~ 30 s. Mg_2SiO_4 forsterite was used as the compositional standard for Mg and Si, while $CaSiO_3$ wollastonite was used for Ca. The grains of bridgmanite, $CaSiO_3$-rich perovskite were analyzed in a focused mode with a beam size of less than 1 μm. The quenched melt was analyzed in a scanning mode larger than the spatial scale of heterogeneity.

Thermodynamic modeling

Among many available thermodynamic approaches that can describe the melting behavior in a multi-component system, we followed that of Liebske and Frost (2012) to maintain consistency with the results for the MgO–$MgSiO_3$ system, which has been studied extensively at high pressures, including lower-mantle pressures. Liebske and Frost (2012) used the chemical potentials given by Lithgow-Bertelloni and Stixrude (2005) and Stixrude and Lithgow-Bertelloni (2011) for the solid phases and by de Koker and Stixrude (2009) for the liquid phases; these papers constructed an internally consistent thermodynamic model, although the equations, parameterization, and parameter set differ slightly from those of Liebske and Frost (2012). For solids, we used the thermodynamic descriptions and parameter sets of Lithgow-Bertelloni and Stixrude (2005) and Stixrude and Lithgow-Bertelloni (2011) based on usability and consistency with other components. For liquids, we followed Liebske and Frost (2012) to maintain consistency with the MgO–$MgSiO_3$ system. We describe all of these equations below for clarification.

Chemical equilibrium is attained when the chemical potentials (μ) of the components become equal between the liquid and solid phases:

$$\mu_Y^{\text{solid}} = \mu_Y^{\text{liquid}}, \tag{1}$$

where μ_Y^{phase} represents the chemical potential of component *Y*, i.e., $MgSiO_3$ or $CaSiO_3$, in the assigned phase. The chemical potentials of solids and liquid are expressed as follows:

$$\begin{aligned} \mu_Y^{\text{phase}} &= \mu_Y^{o,\text{phase}} + RTln\left(a_Y^{\text{phase}}\right), \\ \mu_Y^{\text{phase}} &= \mu_Y^{o,\text{phase}} + RTln\left(X_Y^{\text{phase}}\right) + RTln\left(\gamma_Y^{\text{phase}}\right), \end{aligned} \tag{2}$$

where μ_Y^o, a_Y, X_Y, and γ_Y are the chemical potentials of the endmember, activity, molar concentration, and activity coefficient of component *Y*, respectively. The activity coefficients of solid and liquid are described by the asymmetric regular solution expressions

$$RTln\left(\gamma_{MgSiO_3}^{\text{phase}}\right) = \left[A_o - A_1\left(1-4X_{MgSiO_3}^{\text{phase}}\right)\right]\left(1-X_{MgSiO_3}^{\text{phase}}\right)^2, \tag{3}$$

$$RTln\left(\gamma_{CaSiO_3}^{\text{phase}}\right) = \left[A_o + A_1\left(1-4X_{CaSiO_3}^{\text{phase}}\right)\right]\left(1-X_{CaSiO_3}^{\text{phase}}\right)^2, \tag{4}$$

where A_0 and A_1 are expressed as follows:

Table 2 Experimental summary

Run no.	T (K)	Duration (min)	SM[a]	Phase assemblage
P = 24 GPa				
OS3097	2600(36)	20	Mg90	Bdg + CaPv
			Mg75	Bdg + CaPv
OS3099	2620(38)	15	Mg90	[HT] Melt + Bdg, [LT] Bdg + CaPv
			Mg75	[HT] CaPv, [LT] Bdg + CaPv
OS3095	2700(41)	10	Mg90	Melt
			Mg75	Melt + CaPv
OS3150	3000(46)	5	Mg50	Melt + CaPv

SM starting material, *Bdg*, bridgmanite, *CaPv* $CaSiO_3$-rich perovskite, *HT* high-temperature region, *LT* low-temperature region
[a]See Table 1 for details

$$A_0 = \left(W^{\text{phase}}_{CaSiO_3\text{-}MgSiO_3} + W^{\text{phase}}_{MgSiO_3\text{-}CaSiO_3}\right)/2, \quad (5)$$

$$A_1 = \left(W^{\text{phase}}_{CaSiO_3\text{-}MgSiO_3} - W^{\text{phase}}_{MgSiO_3\text{-}CaSiO_3}\right)/2, \quad (6)$$

where W_{Y-Z} is an interaction parameter between components Y and Z.

Once the chemical potentials of the liquid and solid endmembers are evaluated, we can determine the interaction parameter W by fitting the experimental data to the above equations.

The Gibbs free energy (G) of solid endmembers were determined from the Helmholtz free energy (F) as given by Lithgow-Bertelloni and Stixrude (2005) and Stixrude and Lithgow-Bertelloni (2011):

$$G(P,T) = F(V,T) + PV, \quad (7)$$

$$F(V,T) = F_0(V_0,T_0) + F_{cmp}(V,T_0) + [F_{th}(V,T) - F_{th}(V,T_0)], \quad (8)$$

$$P(V,T) = P_{cmp}(V,T_0) + P_{th}(V,T), \quad (9)$$

where F is composed of a standard-state term (F_0), a compression term (F_{cmp}), and a thermal term (F_{th}). Pressure (P) is composed of a compression term (P_{cmp}) and a thermal term (P_{th}). The compression term is expressed by the following third-order finite-strain (f) model:

$$F_{cmp}(V,T_0) = \frac{9}{2}V_0K_{T_0}f^2 + \frac{9}{2}V_0K_{T_0}(K_{T_0}'-4)f^3 \quad (10)$$

$$P_{cmp}(V,T_0) = (1+2f)^{5/2}\left[3K_{T_0}f + \frac{9}{2}K_{T_0}(K_{T_0}'-4)f^2\right], \quad (11)$$

$$f = \frac{1}{2}\left[\left(\frac{V_0}{V}\right)^{2/3} - 1\right], \quad (12)$$

where V_0, K_{T0}, and K_{T0}' are the volume at a reference state, the bulk modulus, and the first derivative of the bulk modulus, respectively. The thermal term is derived from the Debye model:

$$F_{th}(V,T) = 9nRTD\left(\frac{\theta}{T}\right), \quad (13)$$

$$D(x) = x^{-3}\int_0^x \ln(1-\exp(-t))t^2dt, \quad (14)$$

$$P_{th}(V,T) = \frac{\gamma}{V}(E_{th}(V,T) - E_{th}(V,T_0)), \quad (15)$$

$$E_{th}(V,T) = 9nRT\left(\frac{\theta}{T}\right)^{-3}\int_0^{\frac{\theta}{T}}\frac{t^3}{e^t-1}\,dt, \quad (16)$$

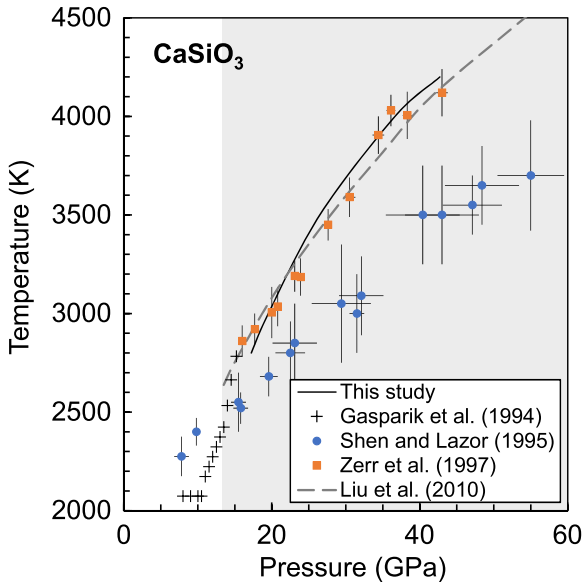

Fig. 1 Melting temperatures of $CaSiO_3$. The black line represents the melting temperatures calculated in this study, the crosses represent the experimental data by Gasparik et al. (1994), the blue circles by Shen and Lazor (1995), the orange squares by Zerr et al. (1997), and the dark gray dashed line represents the molecular dynamics simulation by Liu et al. (2010). The gray region is the stability region of $CaSiO_3$ perovskite at the melting temperatures (Gasparik et al. 1994)

$$\theta = \theta_0\left[1 + 6\gamma_0 f + \frac{1}{2}\left(-12\gamma_0 + 36{\gamma_0}^2 - 18q_0\gamma_0\right)f^2\right]^{1/2}, \quad (17)$$

$$\gamma = \gamma_0\frac{(1+2f)}{(1+6\gamma_0 f)}, \quad (18)$$

where the parameters $F(V_0,T_0)$, V_0, K_{T0}, K_{T0}', θ_0, γ_0, and q_0 were given by Stixrude and Lithgow-Bertelloni (2011).

Table 3 Thermodynamic properties of liquids

	$MgSiO_3$	$CaSiO_3$	MgO
T_0 (K)	1773	3000	3000
V_0 (cm^3/mol)	37.20(6)	45.1(12)	16.46(1)
K_{T0} (GPa)	27.3(2)	22.2(30)	34.0(1)
K_{T0}'	5.7(5)	4.60(17)	4.50(5)
γ_0	0.60(2)	0.73	0.96(2)
γ'	− 1.24(5)	− 1.18(5)	− 0.37(5)
C_v (J/K/mol)	173(2)	146(6)	56(3)
S_0 (J/K/mol)	333(3)	*425(3)*	173.5(20)
F_0 (kJ/mol)	*− 1709.09*	*2282.25*	*− 845.22*
Reference	LF2012	B2015	LF2012

Italicized values were constrained in this study. The others are from literature: LF2012, Liebske and Frost (2012); B2015, Bajgain et al. (2015)

Table 4 Thermodynamic properties of solids

	Bdg	CaPv	Pc
T_0 (K)	300	300	300
V_0 (cm^3/mol)	24.45	27.45	11.24
K_{T0} (GPa)	251(3)	236(4)	161(3)
K_{T0}'	4.1(1)	3.9(2)	3.8(2)
γ_0	1.57(5)	1.89(7)	1.36(5)
q_0	1.1(3)	0.9(16)	1.7(2)
θ_0 (K)	905(5)	796(44)	767(9)
F_0 (kJ/mol)	− 1368(1)	− 1463(8)	− 569

The parameters are from Stixrude and Lithgow-Bertelloni (2011)
Bdg bridgmanite, *CaPv* $CaSiO_3$-rich perovskite, *Pc* periclase

For liquids, we followed Liebske and Frost (2012) to maintain consistency. The expressions of the solid compression terms F_{cmp} and P_{cmp} were also applied to liquids, F_{cmp} and P_{cmp}. The thermal part is expressed as follows:

$$F_{th}(V,T) = -S_0(T-T_0) - C_v\left[T\ln\left(\frac{T}{T_0}\right) - (T-T_0)\right] - C_v(T-T_0)\left[(\gamma_0-\gamma')\ln\left(\frac{V}{V_0}\right) + (\gamma-\gamma_0)\right], \quad (19)$$

$$P_{th}(V,T) = \frac{\gamma}{V}C_v(T-T_0), \quad (20)$$

$$\gamma = \gamma_0 + \gamma'\left(\frac{V}{V_0} - 1\right), \quad (21)$$

where the parameters of $MgSiO_3$ liquid are from Liebske and Frost (2012), except for F_0. For the liquid properties of the $CaSiO_3$ endmember, we used the result of ab initio calculations by Bajgain et al. (2015) by fitting their dataset to the above equations. The F_0 and S_0 of the $CaSiO_3$ liquid were determined by fitting the melting temperatures measured by Zerr et al. (1997), which are consistent with the results of molecular dynamics simulations by Liu et al. (2010) (Fig. 1). The thermodynamic parameters used in this study are summarized in Tables 3 and 4.

The previous study fitted F_0 for standard melting points: MgO, 3070 K at 1 bar; $MgSiO_3$, 2900 K at 25 GPa. We found that the F_0 fitted using the equations defined in the aforementioned methods is slightly different from those reported by previous studies. Nevertheless, we confirmed that we could reproduce the melting temperatures of MgO and $MgSiO_3$ and the MgO–$MgSiO_3$ melting phase relations using the parameters obtained in this study (Fig. 2, Additional file 1: Figures S3 and S4).

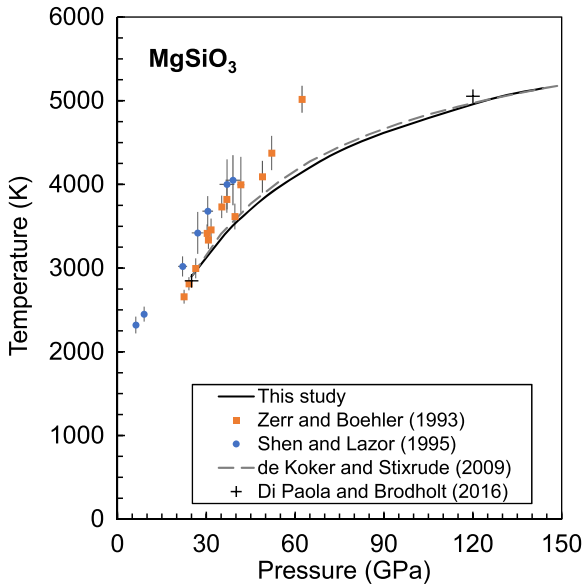

Fig. 2 Melting temperatures of $MgSiO_3$. The black line represents the melting temperatures calculated in this study, the crosses by Di Paola and Brodholt (2016), and the dashed gray line by de Koker and Stixrude (2009). The melting temperatures determined by high-pressure experiments are also plotted: orange squares, Zerr and Boehler (1993); blue circles, Shen and Lazor (1995)

Results and discussion

X-ray diffraction and phase identification

Additional file 1: Figure S5 shows the XRD patterns of the run products. Intense peaks from Re were unavoidably observed in all the patterns due to the small sample sizes in this study. Peaks from bridgmanite were evidently observed in OS3097 and OS3099, indicating that the experiments were performed outside of the garnet stability region, which is consistent with a previous study that reported the phase transformation of a $MgSiO_3$-rich composition from garnet to bridgmanite at 22.4 GPa (Gasparik 1996). Some weak peaks, presumably indexed to bridgmanite, were observed in OS3095 and OS3150 (e.g., Additional file 1: Figure S5e). The bridgmanite is interpreted as quench crystals from melt in the corresponding SEM images as shown later. $CaSiO_3$-rich perovskite was not identified in all the samples since it should be amorphized at the ambient pressure.

Electron microscopic observation and compositional analysis

Figures 3, 4, 5, and 6 show the backscattered electron images of the recovered samples. At 2600 K, the subsolidus phase assemblage of bridgmanite plus $CaSiO_3$-rich perovskite was obtained in both starting compositions (Fig. 3). Bridgmanite contains 5–6 mol% $CaSiO_3$ component, which is higher than that reported by Irifune et al. (2000) at 1773–2173 K, suggesting a positive

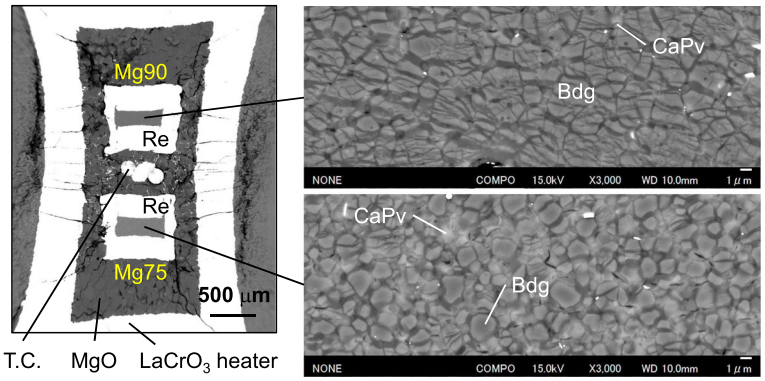

Fig. 3 Backscattered electron images for the samples recovered from high pressure and high temperature (Run No. OS3097). The subsolidus phase assemblage of bridgmanite (Bdg) plus $CaSiO_3$-rich perovskite (CaPv) was observed in both Mg90 and Mg75. T.C., thermocouple

temperature effect on solubility. We did not determine the solubility of $MgSiO_3$ component in $CaSiO_3$-rich perovskite because of its small grain size. At 2620 K, the sample OS3099-Mg90 had a quenched melt with quench textures surrounded by bridgmanite, which is interpreted as the liquidus phase, at the side part of the capsule (Fig. 4). At the central part, the subsolidus phase assemblage of bridgmanite plus $CaSiO_3$-rich perovskite was found. This observation suggests that the axial thermal gradient in the heater has been effectively reduced so that the radial thermal gradient mainly influenced the phase distribution in this sample. In the sample OS3099-Mg75, we observed a segregation of $CaSiO_3$-rich perovskite at the hot side part of the

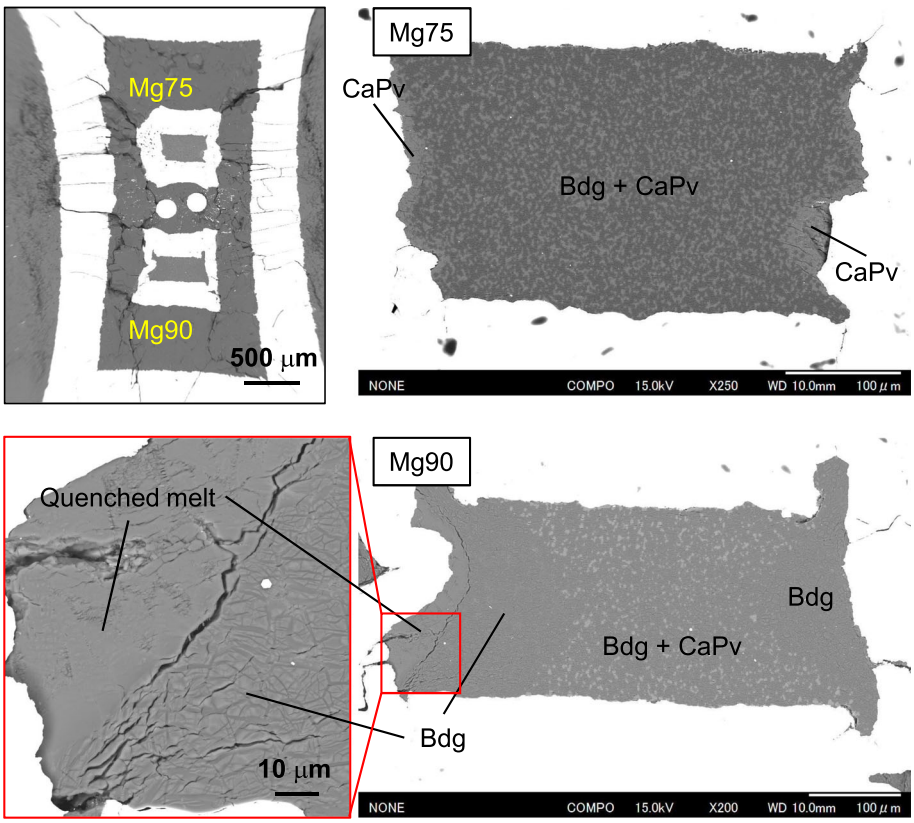

Fig. 4 Backscattered electron images for the samples recovered from high pressure and high temperature (Run No. OS3099). In Mg90, a quenched melt was found at the hottest region surrounded by bridgmanite (Bdg), which is interpreted as the liquidus phase. In contrast, $CaSiO_3$-rich perovskite (CaPv) was found to be segregated in Mg75. We failed to find the melt. The subsolidus phase assemblage was observed at the central (cold) part of both samples

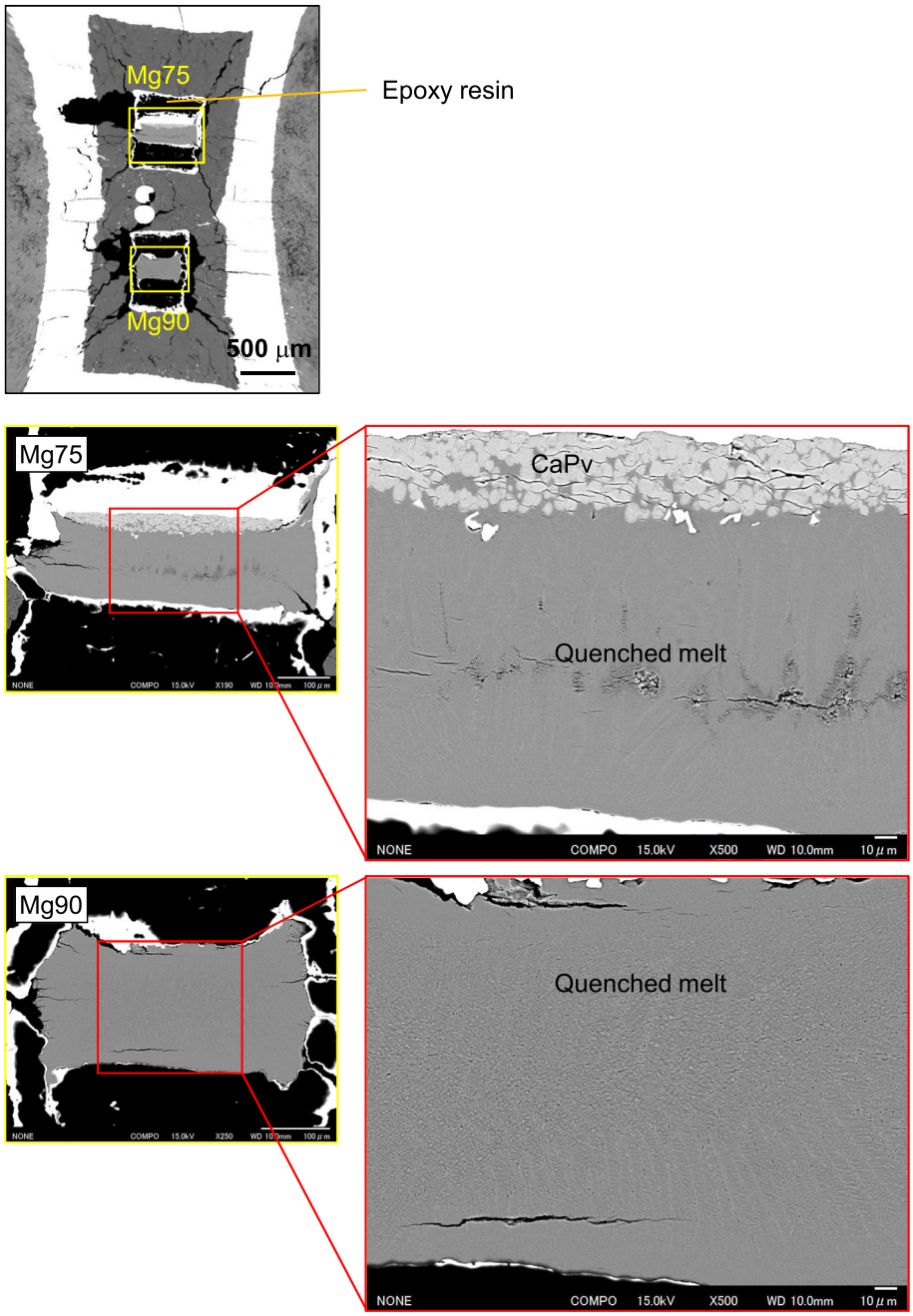

Fig. 5 Backscattered electron images for the samples recovered from high pressure and high temperature (Run No. OS3095). Quenched melts were found at most of the sample areas. In Mg75, the liquidus phase, $CaSiO_3$-rich perovskite (CaPv), was found at the coldest part

capsule (Fig. 4). This $CaSiO_3$-perovskite is interpreted as the liquidus phase, although we failed to find the quenched melt. At 2700 K, the samples were extensively molten, as clearly evidenced by the textures shown in Fig. 5. Both quenched melts exhibited textures similar to that of metal casting: fine grains attached to the mold wall; columnar grains arranged closely in parallel with the direction of cooling heat flow; and granular grains accumulated at the center. The sample OS3095-Mg90 had a bulk composition identical to that of the starting material, supporting a complete melting. In the sample OS3095-Mg75, $CaSiO_3$-rich perovskite, interpreted as the liquidus phase, was observed at the coldest part of the capsule. At 3000 K, the sample OS3150-Mg50 yielded a phase assemblage of $CaSiO_3$-rich perovskite plus melt (Fig. 6), identical to the sample OS3095-Mg75 (Fig. 5). The results of the chemical analyses are summarized in Table 5.

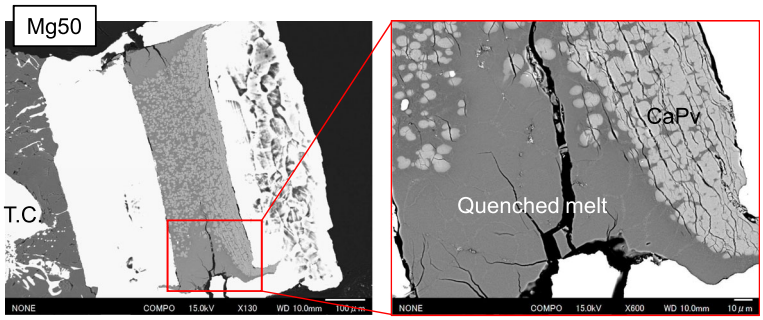

Fig. 6 Backscattered electron images for the sample recovered from high pressure and high temperature (Run No. OS3150-Mg50). A quenched melt was found at the hottest region surrounded by $CaSiO_3$-rich perovskite (CaPv), which is interpreted as the liquidus phase

Melting phase relations in the $MgSiO_3$–$CaSiO_3$ system

The phase relations are summarized in Fig. 7. The solubility of $MgSiO_3$ component into $CaSiO_3$-rich perovskite is much higher than that predicted by theoretical calculations (Jung and Schmidt 2011). This is because Jung and Schmidt (2011) considered a tetragonal structure (I4/mcm) for $CaSiO_3$ perovskite, in addition to their use of oversimplified assumptions, as commented in their paper. Indeed, Komabayashi et al. (2007) showed that $CaSiO_3$ perovskite undergoes a phase transition from tetragonal to cubic above ~ 500 K at ~ 24 GPa. We determined the interaction parameter W^{solid} by fitting our experimental data together with the dataset of Irifune et al. (2000) to the following equations:

$$W^{solid}_{MgSiO_3\text{-}CaSiO_3}\ [kJ/mol] = 108(11) - 0.024(5) \times T\ [K],$$

$$W^{solid}_{CaSiO_3\text{-}MgSiO_3}\ [kJ/mol] = 52(8) + 0.010(4) \times T\ [K].$$

The eutectic point was found to be located at 81–86 mol% $MgSiO_3$ and 2600–2620 K. The interaction parameter W^{liquid} was determined by fitting our experimental data to the following equations:

$$W^{liquid}_{MgSiO_3\text{-}CaSiO_3}\ [kJ/mol] = 1839(741) - 0.59(26) \times T\ [K],$$

$$W^{liquid}_{CaSiO_3\text{-}MgSiO_3}\ [kJ/mol] = -1170(167) + 0.39(6) \times T\ [K].$$

The parameters were estimated using a linear least-squares method weighted by the compositional uncertainty. Therefore, the standard error of the fitting parameter, shown in parenthesis, does not include temperature uncertainty since the dataset from the

Table 5 Chemical compositions of phases in run products

Run no.	SM[a]	Phase[b]	MgO	CaO	SiO_2	Total (wt.%)	Mg	Ca	Si	∑Cation[c]	Mg/(Mg + Ca)
OS3097	Mg90	S-Bdg (48)	37.56(101)	3.07(121)	62.12(76)	102.74(112)	0.915(19)	0.054(21)	1.016(4)	1.984(4)	0.945(22)
	Mg75	S-Bdg (32)	36.45(93)	3.35(86)	61.46(72)	101.25(130)	0.901(16)	0.060(15)	1.020(4)	1.980(4)	0.938(16)
OS3099	Mg90	Melt (9)	33.57(42)	8.49(28)	57.33(86)	99.39(86)	0.864(12)	0.157(6)	0.990(6)	2.010(6)	0.846(5)
		L-Bdg (44)	38.25(106)	2.12(79)	61.04(100)	101.42(171)	0.943(15)	0.038(14)	1.010(3)	1.990(3)	0.962(14)
		S-Bdg (34)	38.26(100)	1.99(60)	60.84(106)	101.09(181)	0.946(13)	0.035(11)	1.009(4)	1.991(4)	0.964(11)
		S-CaPv (28)	4.89(63)	40.58(67)	52.85(67)	98.32(85)	0.140(18)	0.834(17)	1.013(5)	1.987(5)	0.143(17)
	Mg75	L-CaPv (29)	5.34(75)	40.30(83)	52.72(84)	98.36(97)	0.153(22)	0.827(17)	1.010(8)	1.990(8)	0.155(21)
		S-CaPv (33)	5.68(57)	39.90(78)	52.97(64)	98.55(87)	0.161(16)	0.816(16)	1.011(7)	1.989(7)	0.165(16)
		S-Bdg (44)	39.05(66)	1.80(31)	61.89(74)	102.74(121)	0.949(8)	0.031(6)	1.010(3)	1.990(3)	0.968(6)
OS3095	Mg90	Melt (13)	35.49(38)	5.29(13)	58.47(44)	99.24(84)	0.904(4)	0.097(2)	0.999(2)	2.000(2)	0.903(2)
	Mg75	Melt (15)	31.47(46)	10.35(16)	57.63(57)	99.46(112)	0.812(4)	0.192(2)	0.998(2)	2.002(2)	0.809(2)
		L-CaPv (31)	4.39(36)	42.59(58)	53.01(65)	100.00(81)	0.124(10)	0.865(13)	1.005(4)	1.995(4)	0.125(10)
OS3150	Mg50	Melt (21)	28.27(72)	14.57(90)	56.85(40)	99.70(67)	0.737(16)	0.273(18)	0.995(2)	2.005(2)	0.730(17)
		L-CaPv (37)	3.42(43)	43.32(59)	53.52(31)	100.25(48)	0.096(12)	0.878(13)	1.013(3)	1.987(3)	0.099(12)

SM starting material, *S-* subsolidus, *L-* liquidus, *Bdg* bridgmanite, *CaPv* $CaSiO_3$-rich perovskite
[a]See Table 1 for details
[b]Number of electron microprobe analyses is shown in parentheses
[c]Number of oxygen is 3

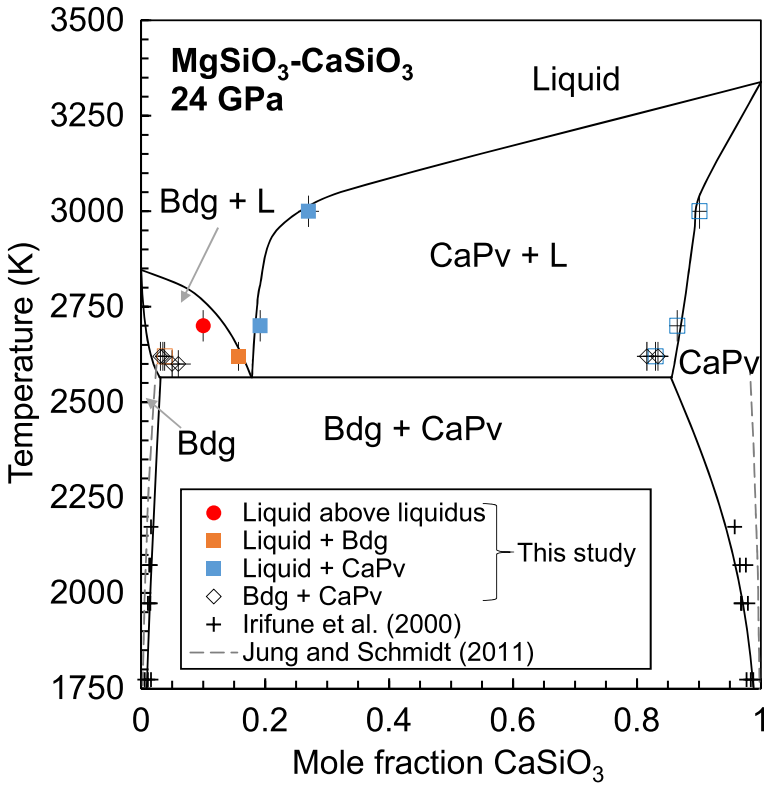

Fig. 7 Melting phase diagram in the $MgSiO_3$–$CaSiO_3$ system at 24 GPa. The filled red circle represents the composition of liquid above liquidus, the filled and open orange squares represent the liquid and coexisting bridgmanite (Bdg), the filled and open blue squares represent the liquid and coexisting $CaSiO_3$-rich perovskite (CaPv), the open diamonds represent the subsolidus phases, the cross symbols represent the subsolidus phases at 25 and 27 GPa reported in Irifune et al. (2000), and the dashed gray line represents the subsolidus phases at 25 GPa reported in Jung and Schmidt (2011)

literature did not describe how the temperature uncertainty was determined. The experimental data suggest that the interaction parameters approach to zero at high temperatures, suggesting an ideal behavior. These empirical (linear) fitting equations should not be extrapolated out from the experimental range. Figure 7 shows the resulting phase diagram from the thermodynamic calculations together with the experimental data. In prohibiting the extrapolation, the uncertainty of the thermodynamic model is described by the deviations from the experimental data (Figs. 1 and 7, Additional file 1: Figure S4).

Conclusions

Melting phase relations in the system $MgSiO_3$–$CaSiO_3$ were determined experimentally at 24 GPa. A thermodynamic model was constructed to reproduce the experimental data. The experimental dataset and the thermodynamic parameters derived in this study serve as the basis for understanding the complicated melting behaviors of the Earth's lower mantle.

The advantage of establishing a thermodynamic model is that the degree of melting can be calculated at a certain P-T in a multi-component system. The seismic observations suggested a degree of melting of < 5–30% in ultra-low velocity zones at the base of the lower mantle (Williams and Garnero 1996). The estimation of the degree of melting depends on the wetting property and the elastic properties of the melt; conversely, these properties depend on the compositions of the melt; thus, they depend on the degree of melting. The degree of melting is also an important parameter in understanding the chemical differentiation during magma ocean crystallization. The melt-solid separation by rheological transition occurs at a crystal fraction of approximately 60% (e.g., Abe 1995). Therefore, it is of great importance to understand the phase relations together with the knowledge of the degree of melting at relevant pressures and temperatures. However, there are some difficulties in obtaining the degree of melting by high-pressure melting experiments under thermal gradients because the observed degree of melting arises from the thermal gradients, not from the phase equilibrium.

Figure 8 shows the eutectic temperatures of the MgO–$MgSiO_3$ system calculated using interaction parameters constrained from the chemical analyses of the recovered diamond anvil cell (DAC) samples (Ohnishi et al. 2017) and those measured directly by

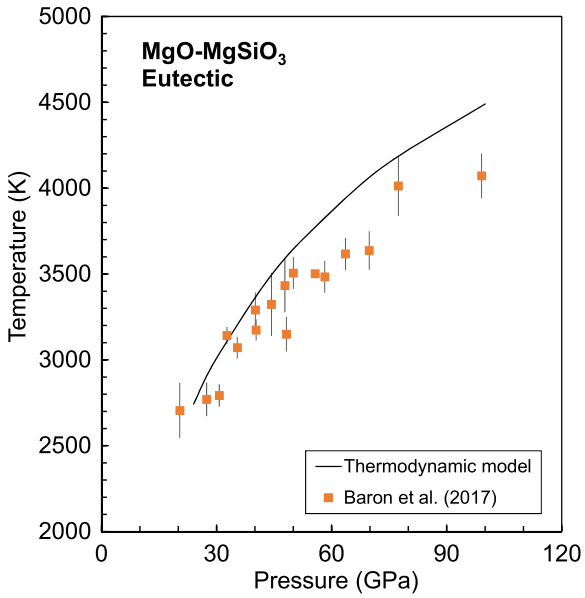

Fig. 8 Eutectic temperatures of the MgO–$MgSiO_3$ system calculated using interaction parameters constrained from chemical analyses of the recovered DAC samples (Ohnishi et al. 2017) and those measured directly by pyrometry in DAC experiments (Baron et al. 2017)

pyrometry in DAC experiments (Baron et al. 2017). As shown in Fig. 8, there is a deviation between these two studies with systematically lower temperatures in Baron et al. (2017). The deviation may have been caused by the inaccuracy of the temperature measurements by the pyrometer, the uncertain wavelength-dependent emissivity of the sample, and the effect of integrated radiation along the thermal gradients in an axial direction. The latter would be serious when transparent materials are used as a sample and pressure medium, resulting in an underestimation of the temperature. Indeed, the melting temperatures of endmembers show large discrepancies among DAC studies even if similar melting criteria were used. On the other hand, chemical analyses of the liquid and solid phases in contact (Ohnishi et al. 2017) present a much more reliable dataset because only an assumption of the local equilibrium is necessary without the information on temperature (it is noted that chemical equilibrium is assumed implicitly when melting temperatures are measured directly). Therefore, constructing the thermodynamic model using the Gibbs free energies of the endmembers by ab initio calculations and phase relations constrained by multi-anvil and DAC experiments combined with chemical analysis should be a promising approach to understand the mineralogy of deep mantle melting and comparisons with observations; however, this approach requires a step-by-step accumulation of relevant phase diagrams.

Additional file

Additional file 1: Figure S1. Pressure calibrations at room temperature (RT) and high temperatures. Fo, Mg_2SiO_4, forsterite; Wd, Mg_2SiO_4 wadsleyite; Rw, Mg_2SiO_4 ringwoodite; Ak, $MgSiO_3$ akimotoite; Bdg, $MgSiO_3$ bridgmanite; Pc, MgO periclase. Pressures of the phase transitions at high temperatures were taken from Morishima et al. (1994), Suzuki et al. (2000), and Fei et al. (2004). The red point at 790 ton, 23 GPa, and 2273 K is 0.55 GPa away from the green curve of 1873 K, which is comparable to the standard deviation of the fitting curves, 0.4 GPa. Figure S2: Heating power-temperature relationships. Figure S3: Melting temperatures of MgO. The black line represents the melting temperatures calculated in this study, and the dashed gray line represents those by de Koker and Stixrude (2009). The melting temperatures determined by high-pressure experiments and ab initio calculations are also plotted: orange squares, Zerr and Boehler (1994); green triangles, Alfe (2005); blue circles, Zhang and Fei (2008); purple squares, Du and Lee (2014); and red squares, Kimura et al. (2017). Figure S4: Melting phase diagram in the MgO–$MgSiO_3$ system at 24 GPa. The black line represents the phase boundary calculated in this study, and the gray line represents that by Liebske and Frost (2012). The experimental data by Liebske and Frost (2012) are also plotted, where the red circle represents the composition of liquid above liquidus, the green squares represent liquid coexisting with periclase (Pc), the orange squares represent liquid coexisting with bridgmanite (Bdg), and the diamonds represent subsolidus phases. Interaction parameter updated by Ohnishi et al. (2017) was used to calculate the phase relations. Figure S5: X-ray diffraction patterns of the run products. The black short bars beneath the curves denote the peak positions of bridgmanite (Bdg) and rhenium (Re). (PDF 1046 kb)

Acknowledgements
We thank Takashi Taniuchi (Ehime Univ.) for discussions and Dr. Toru Shinmei (Ehime Univ.), Dr. Takeshi Arimoto (Ehime Univ.), Dr. Wei Sun (Ehime Univ.), and Dr. Steeve Gréaux (Ehime Univ.) for their assistance in our experiments. We thank the editor and the anonymous reviewers for their constructive comments and suggestions. We thank Dr. Hideharu Kuwahara (Ehime Univ.) and Dr. Chie Kato (Tokyo Tech.) for their assistance in the compositional analyses.

Funding
This work was supported by JSPS KAKENHI Grant Numbers JP15H05470, JP15H05830, and JP25220712.

Authors' contributions
RN and YZ designed the project. YZ and TI designed the experiments. YZ carried out the melting experiments and the chemical analysis. RN analyzed the data. RN and YZ wrote the manuscript. All authors read and approved the final manuscript.

Competing interests
The authors declare that they have no competing interests.

Publisher's Note

Author details
[1]Geodynamics Research Center, Ehime University, 2-5 Bunkyo, Matsuyama, Ehime 790-8577, Japan. [2]Earth-Life Science Institute, Tokyo Institute of Technology, 2-12-1 Ookayama, Meguro, Tokyo 152-8550, Japan.

Received: 13 July 2017 Accepted: 14 November 2017
Published online: 28 November 2017

References
Abe Y (1995) Basic equations for evolution of partially molten mantle and core. In: Yukutake T (ed) The Earth's central part: its structure and dynamics. TERRAPUB, Tokyo, pp 215–235
Alfè D (2005) Melting curve of MgO from first-principles simulations. Phys Rev Lett 94:235701. doi: 10.1103/PhysRevLett.94.235701

Bajgain SK, Ghosh DB, Karki BB (2015) First-principles simulations of CaO and $CaSiO_3$ liquids: structure, thermodynamics and diffusion. Phys Chem Mineral 42:393–404. doi: 10.1007/s00269-014-0730-9

Baron MA, Lord OT, Myhill R, Thomson AR, Wang W, Trønnes RG, Walter MJ (2017) Experimental constraints on melting temperatures in the MgO–SiO_2 system at lower mantle pressures. Earth Planet Sci Lett 472:186–196. doi: 10.1016/j.epsl.2017.05.020

de Koker N, Stixrude L (2009) Self-consistent thermodynamic description of silicate liquids, with application to shock melting of MgO periclase and $MgSiO_3$ perovskite. Geophys J Int 178:162–179. doi: 10.1111/j.1365-246X.2009.04142.x

Di Paola C, Brodholt JP (2016) Modeling the melting of multicomponent systems: the case of $MgSiO_3$ perovskite under lower mantle conditions. Sci Rep 6:29830. doi: 10.1038/srep29830

Du Z, Lee KK (2014) High-pressure melting of MgO from (Mg, Fe) O solid solutions. Geophys Res Lett 41:8061–8066. doi: 10.1002/2014GL061954

Fei Y, Van Orman J, Li J, Van Westrenen W, Sanloup C, Minarik W, Hirose K, Komabayashi T, Walter M, Funakoshi KI (2004) Experimentally determined postspinel transformation boundary in Mg_2SiO_4 using MgO as an internal pressure standard and its geophysical implications. J Geophys Res Solid Earth 109:B02305. doi: 10.1029/2003JB002562

Gasparik T (1996) Melting experiments on the enstatite-diopside join at 70–224 kbar, including the melting of diopside. Contrib Mineral Petrol 124:139–153. doi: 10.1007/s004100050181

Gasparik T (2003) Phase diagrams for geoscientists. An atlas of the Earth's interior, Springer Ed.

Gasparik T, Wolf K, Smith CM (1994) Experimental determination of phase relations in the $CaSiO_3$ system from 8 to 15 GPa. Am Min 79:1219–1222

Hirose K, Fei Y, Ma Y, Mao HK (1999) The fate of subducted basaltic crust in the Earth's lower mantle. Nature 397:53–56. doi: 10.1038/16225

Irifune T (1994) Absence of an aluminous phase in the upper part of the Earth's lower mantle. Nature 370:131–133. doi: 10.1038/370131a0

Irifune T, Miyashita M, Inoue T, Ando J, Funakoshi K, Utsumi W (2000) High-pressure phase transformation in $CaMgSi_2O_6$ and implications for origin of ultra-deep diamond inclusions. Geophys Res Lett 27:3541–3544. doi: 10.1029/2000GL012105

Ito E, Kubo A, Katsura T, Walter MJ (2004) Melting experiments of mantle materials under lower mantle conditions with implications for magma ocean differentiation. Phys Earth Planet Inter 143:397–406. doi: 10.1016/j.pepi.2003.09.016

Jung DY, Schmidt MW (2011) Solid solution behavior of $CaSiO_3$ and $MgSiO_3$ perovskites. Phys Chem Mineral 38:311–319. doi: 10.1007/s00269-010-0405-0

Kimura T, Ohfuji H, Nishi M, Irifune T (2017) Melting temperatures of MgO under high pressure by micro-texture analysis. Nature Comm 8:15735. doi: 10.1038/ncomms15735

Komabayashi T, Hirose K, Sata N, Ohishi Y, Dubrovinsky LS (2007) Phase transition in $CaSiO_3$ perovskite. Earth Planet Sci Lett 260:564–569. doi: 10.1016/j.epsl.2007.06.015

Liebske C, Frost DJ (2012) Melting phase relations in the MgO–$MgSiO_3$ system between 16 and 26GPa: implications for melting in Earth's deep interior. Earth Planet Sci Lett 345:159–170. doi: 10.1016/j.epsl.2012.06.038

Lithgow-Bertelloni C, Stixrude L (2005) Thermodynamics of mantle minerals—I. Physical properties. Geophys J Int 162:610–632. doi: 10.1111/j.1365-246X.2005.02642.x

Liu ZJ, Yan J, Duan SQ, Sun XW, Zhang CR, Guo Y (2010) The melting curve of perovskite under lower mantle pressures. Solid State Comm 150:590–593. doi: 10.1016/j.ssc.2009.12.038

Morishima H, Kato T, Suto M, Ohtani E, Urakawa S, Utsumi W, Shimomura O, Kikegawa T (1994) The phase boundary between α- and β-Mg_2SiO_4 determined by in situ X-ray observation. Science 265:1202–1203. doi: 10.1126/science.265.5176.1202

Ohnishi S, Kuwayama Y, Inoue T (2017) Melting relations in the MgO–$MgSiO_3$ system up to 70 GPa. Phys Chem Mineral 44:1–9. doi: 10.1007/s00269-017-0871-8

Shen G, Lazor P (1995) Measurement of melting temperatures of some minerals under lower mantle pressures. J Geophys Res Solid Earth 100:17699–17713. doi: 10.1029/95JB01864

Stixrude L, Lithgow-Bertelloni C (2011) Thermodynamics of mantle minerals-II. Phase equilibria. Geophys J Int 184:1180–1213. doi: 10.1111/j.1365-246X.2010.04890.x

Suzuki A, Ohtani E, Morishima H, Kubo T, Kanbe Y, Kondo T (2000) In situ determination of the phase boundary between wadsleyite and ringwoodite in Mg_2SiO_4. Geophys Res Lett 6:803–806. doi: 10.1029/1999GL008425

Williams Q, Garnero EJ (1996) Seismic evidence for partial melt at the base of Earth's mantle. Science 273:1528. doi: 10.1126/science.273.5281.1528

Zerr A, Boehler R (1993) Melting of (Mg, Fe) SiO_3-perovskite to 625 kilobars: indication of a high melting temperature in the lower mantle. Science 262:553–556. doi: 10.1126/science.262.5133.553

Zerr A, Boehler R (1994) Constraints on the melting temperature of the lower mantle from high-pressure experiments on MgO and magnesiowustite. Nature 371:506–508. doi: 10.1038/371506a0

Zerr A, Serghiou G, Boehler R (1997) Melting of $CaSiO_3$ perovskite to 430 kbar and first in-situ measurements of lower mantle eutectic temperatures. Geophys Res Lett 24:909–912. doi: 10.1029/97GL00829

Zhang J, Liebermann RC, Gasparik T, Herzberg CT (1993) Melting and subsolidus relations of SiO_2 at 9–14 GPa. J Geophys Res 98:19785–19783. doi: 10.1029/93JB02218

Zhang L, Fei Y (2008) Melting behavior of (Mg, Fe) O solid solutions at high pressure. Geophys Res Lett 35:L13302. doi: 10.1029/2008GL034585

Zhou Y, Irifune T, Ohfuji H, Sinmei T, Du W (2017) Stability region of $K_{0.2}Na_{0.8}AlSi_3O_8$ hollandite at 22 GPa and 2273 K. Phys Chem Mineral 44:33–42. doi: 10.1007/s00269-016-0834-5